Star formation in the bar of NGC 2903

Gergö Popping
Supervisors: Isabel Pérez-Martin & Almudena Zurita Muñoz

24th October 2008

Abstract

We have obtained Hα photometry of HII regions in the bar of NGC 2903. Equivalent widths have been analysed carefully as a function of position with respect to the bar major axis and the nucleus. We found that the EW of the regions is randomly distributed as a function of radial distance with respect to the galaxy nucleus. We did find differences in the EW as a function of distance to the bar major axis. A group of low EW regions is located within a perpendicular distance of 45 arcsec from the bar major axis at the leading side, whereas a group of mainly high EW regions is located further out from the bar major axis at the leading side. This is a different trend than was found before for NGC 1530.
We also carried out a study on the star formation history in the bar of NGC 2903, using a g'-z' dust indicating colourmap, IR, UV and CO data. We found a large UV region (tracing star formation up to 1 Gyr) without a counterpart in Hα and not correlating with the bar morphology. Hα traces places where bar dynamics favours SF, therefore we conclude that the SF up to 1 Gyr ago as traced by the UV, is not associated with the bar dynamical features as traced by the gas. Since we do not see older population stars in this regions as well, this might indicate that the bar has been formed less than 1 Gyr ago.

Contents

1 Introduction

The bachelor research project is the final part of the Bachelor in astronomy at the Kapteyn Institute. This report is about the research I did on the star formation in the bar of NGC 2903.

Bars are ideal places for studying the physical parameters that trigger and inhibit star formation. Lots of possibilities arise, as bars show extreme physical conditions, with strong shear, shocks, high non-circular velocities (Pence and Blackman 1984; Athanassoula 1992; Reynaud and Downes 1998; Giammanco et al. 2004) and significant magnetic field strength (Beck 2002).
HII regions are volumes of ionized gas surrounding one or several young massive stars. These young stellar clusters produce the HII regions via ionization by their emitted Lyman continuum photon flux. Since HII regions are bright in Hα and more easily observed than the young stellar clusters producing them, HII regions are commonly used as tracers of recent star formation.
Only a few papers give insight on the location, distribution and properties of star forming regions with respect to bars. Places and parameters providing suitable conditions for SF in bars are not yet well understood. (Martin and Friedli 1999) and (Verley et al. 2007) have classified barred galaxies in 3 groups depending on the spatial distribution of the recent SF in bars as traced by the Hα emission line:

1. HII regions are distributed along the bar.
2. HII regions are located in the nuclear or circumnuclear region with little or no Hα emission from the bar.
3. HII regions are located in the nuclear and circumnuclear region as well as in the bar.

The second distribution seems to be more common. Martin and Friedli (Martin and Friedli 1999) suggest an evolutionary sequence of the bar defined by the different stages of Hα emission distribution. First, the SF is distributed along the bar. Then, due to inflow of the gas to the galaxy centre, the gas is depopulated from the bar.
Commonly, one can see a misalignment up to $\sim 30^\circ$ between Hα emission detected along bars and stellar and molecular gas emission, the Hα bar leading the stellar one (Martin and Friedli 1999; Verley et al. 2007; Rozas et al. 2000). This misalignment confirms that internal dynamics play a large role on SF.
Zurita and Pérez (2008) found for NGC 1530 that HII regions are present both in the leading (ahead of the bar dust lane with respect to its rotational direction) and the trailing (behind the bar dust lane with respect to its rotational direction) part of the bar with respect to the bar dust lanes. They

were the first to do a study on the Hα equivalent width as a function of distance to the bar major axis and found differences in the Hα equivalent width of the HII regions, depending on location. They found HII regions with low Hα equivalent widths at the leading side of the bar dust lane. As Hα equivalent width is a good indicator of star forming activity, this suggests star formation to take place in the trailing side of the bar of NGC 1530, where high gas density is present, but also low shear and low relative velocity with respect to the bar. This is in disagreement with the common understanding of star formation in bars and again shows the importance of taking bar dynamics into account.
The purpose of this research is to extend the study on the HII regions and get a better understanding of star formation with respect to the dynamical features of the bar. We will catalogue HII regions in the bar of NGC 2903 and determine their fluxes and also Hα equivalent widths of the catalogued regions will be derived. The equivalent widths of the HII regions will be compared as a function of distance to the bar major axis and radial distance to the nucleus. By use of multiple wavelength data (IR, UV, CO) obtained from other survey programs we will try to discern the star formation history. NGC 2903 was chosen for this research for a number of reasons. It is a close by, isolated SBd galaxy which allows us to observe with high spatial resolution. It shows a symmetric strong bar considered typical for this class of galaxies. Previous less deep observations have shown lots of Hα emission along the bar and not only to the end of the bar and nuclear region (Sheth et al. 2002). Together with available CO, Spitzer and GALEX data this galaxy is an ideal object for the study on star formation in bars.

First, the observations and data reduction will be described (Sec. 2). Then, we will present the analysis and results of the HII region catalogue and equivalent width determination (Sec. 3). We will discuss the results (Sec. 4) and also discuss the multiple wavelength study (Sec. 5). In Sec. 6 our conclusions are given.

2 Observations and data reduction

2.1 Hα imaging

For our research we used Hα images observed by me in October 2007 with the Wide Field Camera of the 2.5 m Isaac Newton Telescope at Roque de los Muchachos Observatory, La Palma, Spain as a part of the Observational Techniques course. The camera consists of 4 thinned EEV 2kx4k CCDs. The CCDs have a pixel size of 0.33"/pixel, covering 34.2 arcmins in the sky. We assumed a HII region to have a typical luminosity of $10^{38.5}$ erg s^{-1}. Combining this with the distance to the galaxy of 11.6 Mpc and a typical size of a HII region of 200 pc, we deduced an exposure time of 3600s through a 95 Å width Hα filter and 750s through an R-band broad band filter to get a S/N ratio of 13 (Table 1). This S/N ratio ensures observations good enough for the detection of HII regions of the assumed typical luminosity. The R-band image is used for subtracting the continuum that is contained in the Hα band. We acquired flatfield images for flatfield correction and bias images for bias correction. Also spectroscopic standard stars were observed for fluxcalibration of the Hα image. Unfortunately, this was done in non photometric conditions, therefore these image were not used in the end.
We carried out the data reduction using IRAF[1]. Overscan subtraction and bias and flatfield correction were performed on all the images. To do this we used the `ccdproc` and the `imarith` tasks. We subtracted the sky from

[1]IRAF is distributed by the National Optical Astronomy Observatories, which is operated by the Association of Universities for Research in Astronomy, Inc. (AURA) under cooperative agreement with the National Science Foundation.

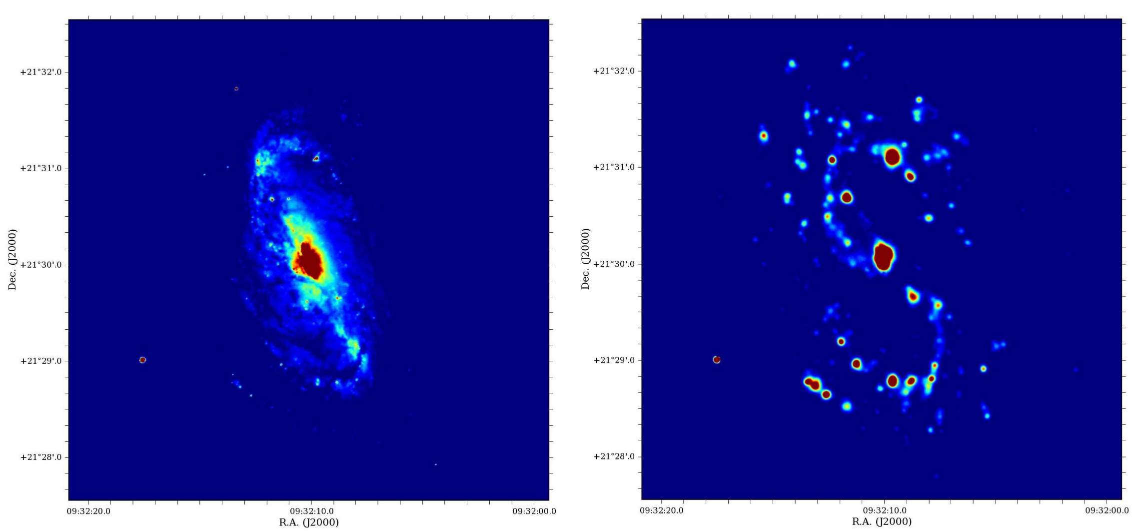

Figure 1: R-band and Hα continuum subtracted image of NGC 2903.

the images and then aligned and combined them using the `imalign` and `imcombine` tasks. For the sky subtraction we used an IRAF script. This script calculates the mean of the sky on many positions and from this creates a sky map using a first order polynomial. We needed a first order polynomial since there was a clear sky gradient in the field. This sky map was then subtracted from the original image.

The continuum subtraction from the Hα image was done as described by Relaño et al. (Relaño et al. 2005). One assumes the field stars to have no Hα emission and therefore their flux to be the same in the Hα (ON-band) as in the R-band (OFF-band) images. With this assumption we can calculate the ratio n of the integrated fluxes between the ON- and OFF-band. By multiplying the OFF-band with this ratio, we scale this band to the ON-band. Subtracting the new obtained image from the ON-band, gives us an Hα image free of continuum emission.

We used 11 foreground stars to subtract the continuum and found a ratio $n = 0.343 \pm 0.02$. Then we made several continuum subtracted images using ratios ranging from 0.325 to 0.35. After inspection we used a value of 0.34 for the subtraction. The R-band and obtained Hα continuum subtracted images can be seen in Figure 1. One clearly sees the Hα to be located in a smaller range than the continuum and the Hα to have clear peaks whereas the continuum mostly shows diffuse emission.

The astrometry was done on the Hα images using the `ccmap` package within IRAF. We determined the position of foreground stars using SDSS[2] observations. Our calibration has an accuracy of 0.39". Since the observations were made during non photometric conditions, the observed spectroscopic standard stars showed large variability's during the night and were not usefull. To do the flux calibration we used earlier reported fluxes for HII regions of NGC 2903.

This was done by aperture photometry on 13 HII regions previously studied by Mayya (1994). We compared the flux reported by Mayya with our measured flux (in ADU) for each of the regions. Then we made a least square fit trough the calculated conversions of all the regions. This gave us a Hα-luminosity of 2.33e-19 $\pm$ 4e-20 erg s^{-1} cm^{-2} count^{-1} (Fig. 2). By multiplying our Hα continuum subtracted image with this number, we obtained our flux calibrated Hα image.

The bandwith of the Hα filter also contains emission from [NII] at the redshifted wavelengths of the [NII] λ 6548Å and [NII] λ 6584Å emission lines. A correction for this requires spectroscopic information for all the HII regions. Unfortunately, there is no spectroscopic information available for the HII regions in the bar of NGC 2903. Therefore the Hα luminosities given in this report also include the [NII] lines. The catalogued HII regions de-

[2]Sloan Digital Sky Survey: Survey to obtain detailed optical images covering more then a quarter of the sky, and a 3d map of about a million galaxies and quasars. www.sdss.org

Table 1: log of observations

Band	Date	Filter	Exp. Time	Seeing
Hα	29 Oct 2007	WFCH6568	3x1200s	1.6”
R	30 Oct 2007	HARRIS R	3x250s	2.1”

scribed by Mayya (1994) also contain [NII] lines.
The typical [NII]/Hα ratio for extragalactic HII regions of solar metallicity is approx. 0.33. Therefore an approximate correction of 25% should be applied to the Ha fluxes and equivalent widths reported here to obtain the Ha emission alone. We assumed the Hα to have an optical depth of 2.4, as derived by Calzetti for starburst galaxies Calzetti et al. (1994).

2.2 Other imaging data

Beside the obtained Hα images, other images were used. We created a g’-z’ colour map using SDSS data, this is described in section 2.3. To perform the multi wavelength study we used UV data observed by the GALEX survey, IR data obtained by the Spitzer survey program and CO data kindly provided to us by Ute Lisenfeld[3]. The images were already reduced. A more detailed description on the survey programs and images is provided in section 5.

2.3 Colour Map

Colour maps can be used to give insight in the dust distribution of a galaxy. We created a g’-z’ colourmap using SDSS data. The g-band is sensitive to young stars and is heavily influenced by dust. The z’ band is less sensitive to young stars and is not as much influenced by dust. Subtracting these two creates a map that gives an indication on the dust distribution, where the low magnitudes represent the dust.
First we subtracted the sky emission of both images to make sure that only emission from the galaxy is included. Since they had the same spatial resolution, we did not have to correct for this. Then we converted the counts into fluxes as described for the SDSS data release:

$$\frac{f}{f_0} = \frac{counts}{10^8 * f_{20}}$$

f_{20} is given in the header of the SDSS observations. The obtained fluxes were converted to magnitudes by

$$m = -2.5log_{10}(\frac{f}{f_0})$$

By subtracting the z’ band from the g’ band, the colourmap was obtained (Fig. 7). The morphology of the g’-z’ colourmap is discussed in section 5.1.

[3]Dep. Física Teórica y del Cosmos, Universidad de Granada

3 Analysis

3.1 HII region catalogue

The HII region catalogue in the bar zone of the galaxy (ie. determination of location, size, fluxes and luminosity of HII regions) was made using GAIA[4]. As selection criteria we used that the area of an image feature must at least be larger than the spatial resolution of the image. Circular or elliptical apertures were plotted around the regions, then the flux was determined by integrating over the aperture. A total of 34 regions were catalogued in the bar of the galaxy, excluding the nuclear region (Fig. 3). The nuclear region was excluded, since the spatial resolution did not allow us to observe separated HII regions, only one big nuclear sized region.
The produced catalogue is presented in table 2. The description of the table is as follows.
(1) ID: HII region number.
(2)-(3) RA, DEC: Position of the HII regions, along right ascension and declination in time (hh:mm:ss) and degrees (○,′,″) respectively.

[4]GAIA is a derivative of the Skycat catalogue and image display tool, developed as part of the VLT project at ESO. Skycat and GAIA are free software under the terms of the GNU copyright.

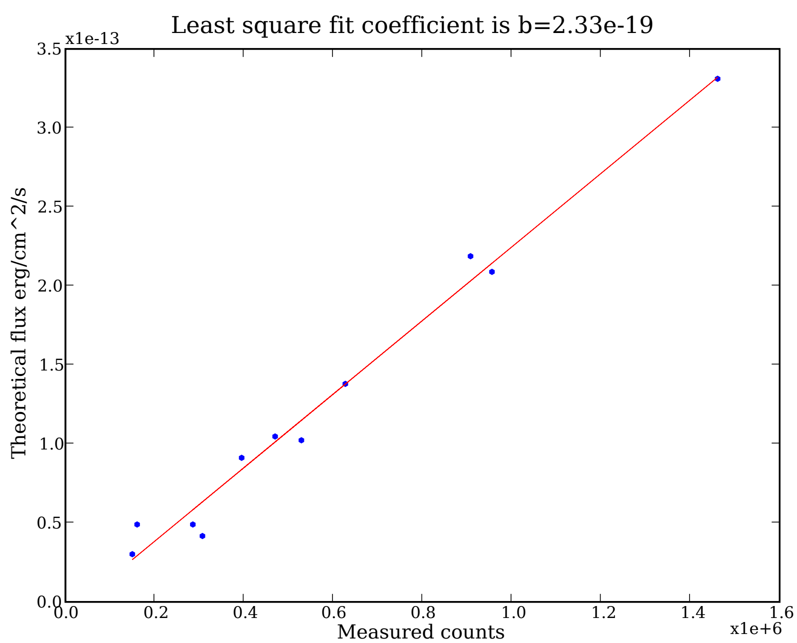

Figure 2: Calibration of the Hα image. In red the least square fit is shown.

(4) Radius: The radius of the major axis of the aperture in arcsec.
(5) Eccen.: The eccentricity of the selected aperture.
(6) Angle: The angle in degrees under which the aperture is rotated clockwise with respect to the right ascension axis.
(7) log(F_{H_α}): logarithm of the observed Hα flux in erg s^{-1} cm^{-2}.
(8) log(L_{H_α}): logarithm of the Hα luminosity in erg s^{-1}.
Figure 4 is a histogram of the found Hα fluxes. The histogram shows most HII regions have a flux -14.2 < log $F_{H\alpha}$ < -13.0 erg cm^{-2} s^{-1}.

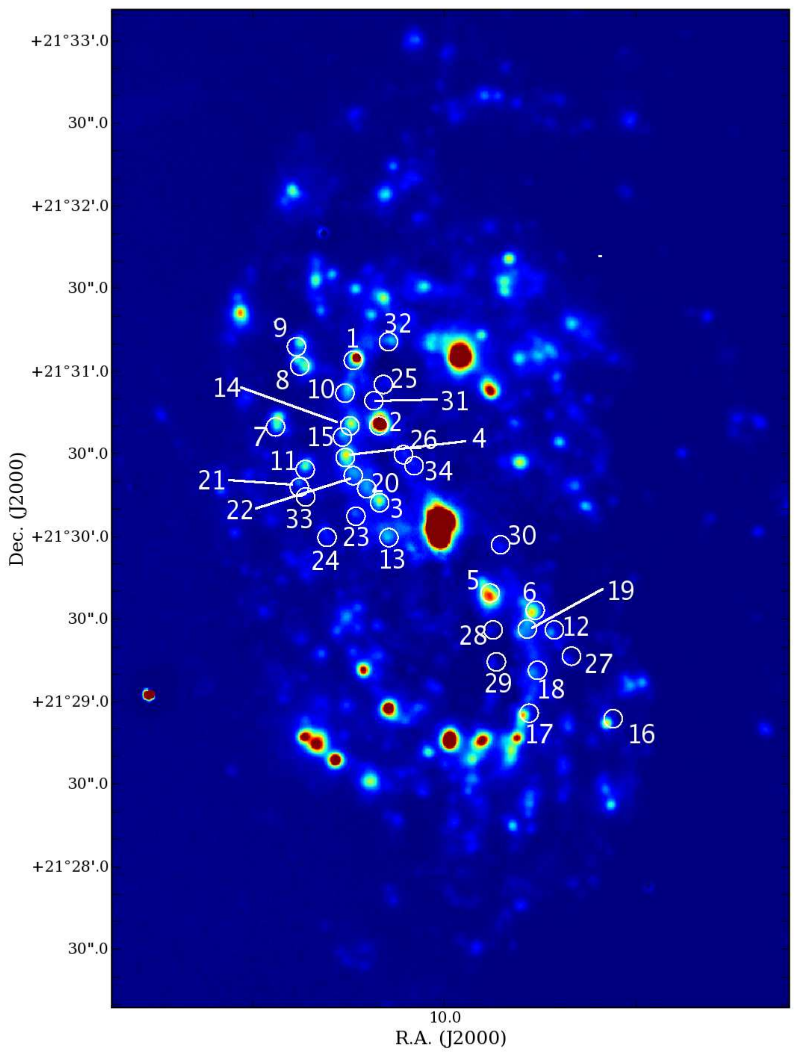

Figure 3: Hα (in arbitrary units) image of NGC 2903 with the representation of the catalogued HII regions.

Table 2: The catalogued Hα regions

ID	RA	DEC	Radius (")	Eccen.	Angle	$\log(F_{H_\alpha})$	$\log(L_{H_\alpha})$
1	2	3	4	5	6	7	8
1	09:32:12.34	21:31:04.96	3.1	0	90	-12.99	39.21
2	09:32:11.67	21:30:41.03	5.23	0.51	158	-12.57	39.63
3	09:32:11.63	21:30:13.10	3.17	0	0	-13.27	38.93
4	09:32:12.54	21:30:29.50	3.0	0	0	-13.24	38.97
5	09:32:07.77	21:29:40.25	7.57	0.78	-25	-12.68	39.52
6	09:32:07.59	21:29:33.89	3.1	0	0	-13.17	39.03
7	09:32:14.36	21:30:40.71	4.23	0.68	6	-13.23	38.98
8	09:32:13.73	21:31:02.77	5.23	0.8	-48	-13.12	39.09
9	09:32:13.82	21:31:09.99	2.33	0	0	-13.55	38.66
10	09:32:12.55	21:30:52.95	4.17	0.77	10	-13.38	38.82
11	09:32:13.59	21:30:25.14	2.93	0.62	45	-13.51	38.70
12	09:32:07.10	21:29:26.53	2.03	0	90	-13.86	38.34
13	09:32:11.41	21:30:00.27	2.7	0	90	-13.54	38.67
14	09:32:12.44	21:30:40.86	3.0	0	0	-13.29	38.92
15	09:32:12.61	21:30:37.04	2.23	0	0	-13.69	38.52
16	09:32:05.57	21:28:54.30	2.8	0	0	-13.39	38.82
17	09:32:07.74	21:28:56.31	2.9	0	90	-13.26	38.95
18	09:32:07.57	21:29:11.97	2.6	0	90	-13.65	38.55
19	09:32:07.80	21:29:27.20	3.57	0	0	-13.33	38.88
20	09:32:11.97	21:30:18.14	2.87	0.85	3	-13.76	38.45
21	09:32:12.33	21:30:23.05	2.7	0.78	108	-13.74	38.47
22	09:32:13.76	21:30:18.62	1.9	0	0	-14.00	38.21
23	09:32:12.28	21:30:08.27	2.0	0	90	-13.98	38.22
24	09:32:13.03	21:30:00.47	4.27	0.87	-16	-13.83	38.38
25	09:32:11.55	21:30:56.30	1.67	0	0	-14.34	37.87
26	09:32:11.05	21:30:30.46	2.0	0	0	-14.07	38.13
27	09:32:06.68	21:29:17.18	1.77	0	0	-14.28	37.92
28	09:32:08.70	21:29:26.75	1.57	0	0	-14.60	37.61
29	09:32:08.62	21:29:14.80	2.33	0	0	-14.18	38.03
30	09:32:08.50	21:29:57.37	3.03	0.84	-53	-14.08	38.12
31	09:32:11.82	21:30:50.26	2.13	0	0	-14.10	38.11
32	09:32:11.44	21:31:11.62	2.33	0	90	-13.68	38.52
33	09:32:13.57	21:30:15.00	1.77	0	90	-14.19	38.02
34	09:32:10.73	21:30:26.53	3.37	0.9	-44	-13.99	38.22

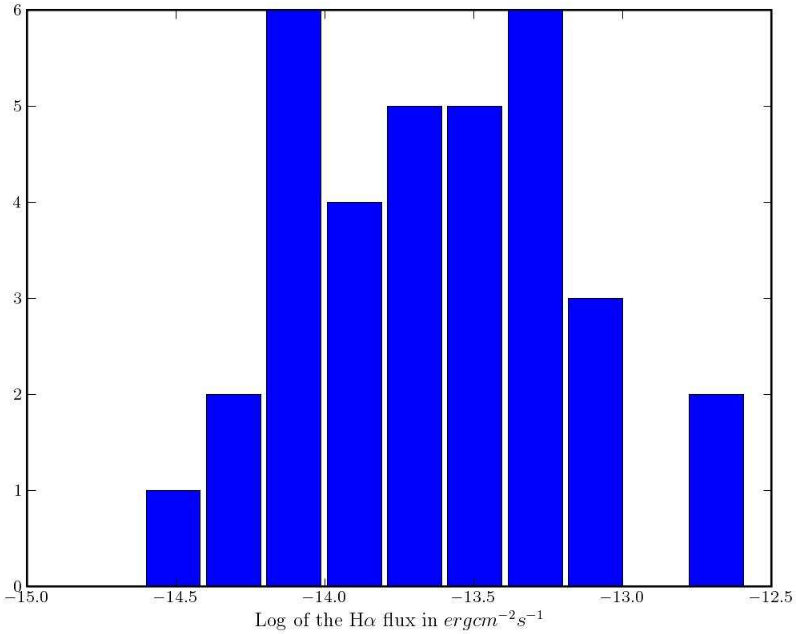

Figure 4: Histogram of the Hα flux. Most of the regions lie within -14.2 < log F_{H_α} <-13.0 erg cm^{-2} s^{-1}

3.2 Hα equivalent width

Equivalent widths are good indicators of the strength of an emission line. It gives a measurement of the emission line flux with respect to the emission from the continuum for a given source. Determining them however is a complex procedure. In the case of Hα emitters in a galaxy, it is necessary to take into account the continuum emission from the underlying population of stars in the galaxy disk. First some general explanations on Hα equivalent widths and its calculation method will be given. Then we will describe our methods for calculating the underlying continuum and the determination of the widths themselves.

3.2.1 Calculating equivalent widths

The Hα equivalent width is a measure of the intensity of Hα. It stands for the relative amount of ionizing and continuum photons emitted by the stellar cluster associated to the HII region:

$$EW_{H\alpha} = \frac{F_{H\alpha}\ (\mathrm{erg\ s^{-1}\ cm^{-2}})}{F_{cont}\ (\mathrm{erg\ s^{-1}\ cm^{-2}\ \AA^{-1}})}$$

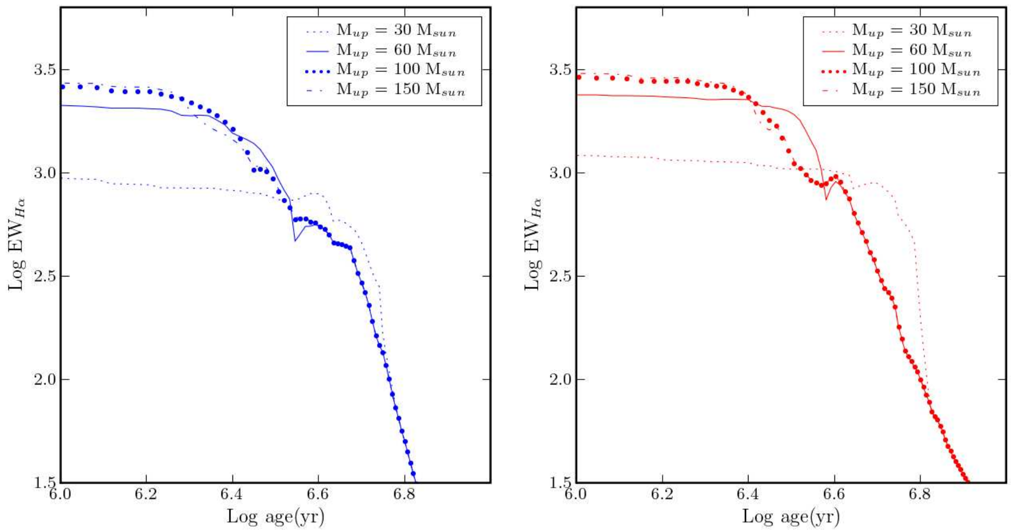

Figure 5: Evolution of H_α equivalent width as function of age predicted by the *Starburst99* model. Left represents metallicity $Z = Z_\odot$, right $Z = 0.5\ Z_\odot$. IMF upper masses in the range 30 $M_\odot$ to 150 $M_\odot$ have been assumed. At log age (yr) > 6.4 the age seems the only dominant factor affecting log EW_{H_α}.

The EW is dependant on dust, since it can extinguish the ionized photons and therefore decrease the observed $EW_{H\alpha}$. The initial mass function (IMF), metallicity and the evolutionary status of the star also can have an influence on the observed $EW_{H\alpha}$. Evolutionary synthesis models can give insight into the dominant factor. We used the *Starburst99* model (Leitherer et al. 1999). This model is optimized to reproduce properties of galaxies with active star formation.
Figure 5 shows the outcome of a *Starburst99* simulation. Different IMF upper mass limits ranging from 30 $M_\odot$ to 150 $M_\odot$ have been assumed, as well as metallicity $Z = 0.5\ Z_\odot$ and $Z = Z_\odot$. The left figure represents metallicity $Z = Z_\odot$, the right one $Z = 0.5\ Z_\odot$. The model assumes a total stellar mass of $1 \times 10^6 M_\odot$, a burst of star formation and it uses the Geneva stellar evolutionary tracks with high mass loss.
One can clearly see that metallicity and IMF have a large impact on log EW_{H_α} for ages ≤ 2.5 Myr (log age (yr) = 6.4). At older ages the EW is independent on metallicity an IMF, this indicates age to be the dominant factor affecting log EW_{H_α} for older star forming regions.

To determine the equivalent width the following equation is used:

$$EW_{H\alpha} = \frac{F_{H\alpha}}{F_R/W_{H\alpha}}$$

$F_{H\alpha}$ and F_R are the Hα and continuum fluxes, as measured in the Hα continuum subtracted and SDSS R-band image respectively. To measure the flux in the SDSS R-band image, we first scaled this image to our OFF band image. $W_{H\alpha}$ is the bandwidth of the Hα filter. As explained in sect 2.1 our continuum image is scaled to the narrowband image. The bandwidth term is introduced to normalise the R-band flux to flux per Å.

3.2.2 Determination methods for the underlying continuum

When measuring the equivalent width, we are only interested in the radiation from the ionizing cluster. However, when measuring the broad band continuum we measure both radiation from the ionizing cluster and underlying emission from the galaxy. Therefore it is necessary to subtract this underlying continuum. We used two different methods to do this. For both we assumed the HII regions to be transparent to the underlying radiation. For the first method we drew an annulus in the continuum image around each ionizing cluster with an inner radius equal to the effective radius of the HII region. The annulus had a width of 5". Then for each region we computed the average flux per pixel squared within the annulus. This value was used to subtract the underlying continuum from the measured flux within the aperture. We masked all the HII regions to avoid contamination from continuum emission from nearby HII regions located in our annuli. For some regions, however, the continuum in the annulus is brighter than within the aperture. This leads to a underestimation of the continuum, and is generally due to strong spatial variation of the disk continuum emission in small scales.

For the second method we used growth curves. In most apertures the continuum is less extended than the Hα, therefore the local background can be obtained within the HII region area as defined by its Hα emission. We derived averaged surface-brightness profiles with increasing radius. Then for each region we selected a radial range not contaminated by the ionizing cluster. We used this range to determine the local background. The main problems of this method are that it does not deal with elliptical apertures and multiple peaks in the continuum.

3.2.3 Determining the Hα equivalent width

For determining the Hα equivalent width we discarded all the regions with a very diffuse continuum emission. They show no clear peak and therefore it

is hard to find a proper value for the continuum. We used both continuum emission methods to calculate the Hα equivalent widths for the remaining regions. For each region we calculated for both methods the relative error in the found EW. We discarded the EWs with a relative error larger than 20%.
For regions 2, 3, 13, 15, 17, 19 this resulted in discarding the whole regions, since both calculation methods gave a relative error larger than 20%. Though the errors in both methods were smaller than 20%, region 9 showed a large difference between the two calculated EWs. We chose to use the growthcurve value, since the surrounding of region 9 in the continuum band shows a large variability in emission. The growthcurve method deals better with this, as it calculates the underlying continuum emission within the aperture. For the remaining regions we calculated the EW by taking the mean of the results of both methods.
The results of the equivalent width determination for the catalogued regions are presented in table 3. For the width of the narrowband filter we used 95 Å. The table columns show: 1) the HII region ID, 2) the EW in Å as calculated with the growthcurve method, 3) the error by use of the growthcurve method, 4) the EW in Å as calculated with the annulus method, 5) the error by use of the annulus method, 6) method by which the final EW was calculated, 6) the final EW, 7) the final error on the EW.

Table 3: Hα equivalent widths of the catalogued HII regions.

ID	$\log(\mathrm{EW})_{growthcurve}$ (Å)	$\mathrm{Error}_{growthcurve}$	$\log(\mathrm{EW})_{annulus}$ (Å)	$\mathrm{Error}_{annulus}$	Used Method	Final EW (Å)	Error
1	2	3	4	5	6	7	8
1	2.36	0.32	2.47	0.46	Mean	2.41	0.39
2	3.16	0.75	3.35	0.89	Discarded	-	-
3	nan	nan	3.34	1.34	Discarded	-	-
4	2.82	0.53	2.94	0.68	Growthcurve	2.82	0.53
5	2.6	0.46	2.38	0.40	Mean	2.49	0.43
6	2.93	0.50	2.94	0.56	Mean	2.94	0.53
8	2.87	0.53	2.88	0.68	Growthcurve	2.87	0.53
9	2.51	0.18	2.99	0.55	Growthcurve	2.51	0.18
10	2.3	0.42	2.73	1.03	Growthcurve	2.30	0.42
11	2.78	0.27	3.12	0.56	Mean	2.95	0.41
12	2.08	0.13	2.62	0.57	Growthcurve	2.08	0.13
13	2.96	0.99	2.36	0.60	Discarded	-	-
14	2.35	0.28	2.99	0.93	Growthcurve	2.35	0.28
15	2.9	0.66	3.00	1.12	Discarded	-	-
16	3.09	0.40	3.03	0.39	Mean	3.06	0.39
17	3.33	1.01	2.84	0.89	Discarded	-	-
19	2.52	0.53	2.82	0.9	Discarded	-	-
24	2.71	0.45	2.40	0.43	Mean	2.56	0.44

4 Discussion

4.1 Hα equivalent widths

4.1.1 EW with respect to bar dust lanes

The equivalent widths show a wide variety in their values (Figure 6) ranging from log 2.08 to 3.06 Å. Two peaks can be seen, one around log EW 2.4, the other around log EW 2.8. Using the *Starburst99* model we can set the age range to run from 2 to 5.6 Myr, assuming that the only factor affecting the EW difference is the age.
Figure 7 shows the HII regions for which the EW was calculated on top of the obtained g'-z' colourmap. Large values represent the dust regions. A dust lane is visible on both sides of the nucleus. Faint dust spurs are visible on the trailing side of both lanes. The blue line represents the bar as defined with the Spitzer 3.6 micron data (sec. 4.1.2).
Except for regions 12 and 24 one sees the low EW regions to be located more close by to the bar dust lane than the high EW regions. This is in contrary with Zurita and Pérez (2008), who found the opposite for NGC 1530. We can conclude from this image that starburst did not take place at the same time through the galaxy, but there were several burst.

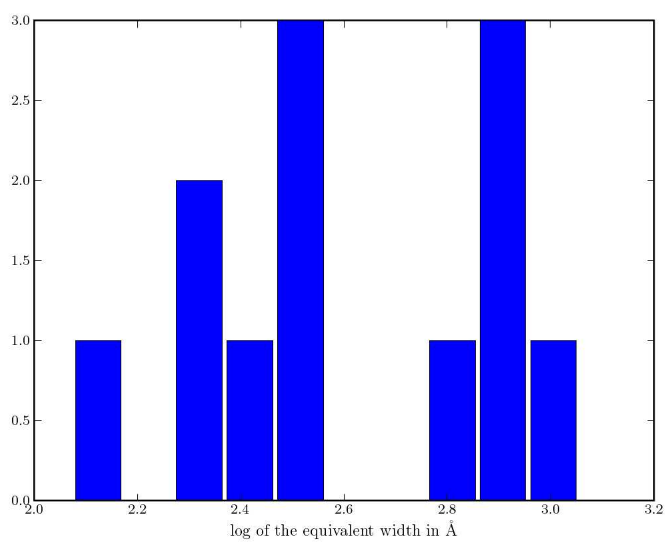

Figure 6: Histogram of the equivalent width values. A wide distribution of EW is seen, indicating both older as younger HII regions.

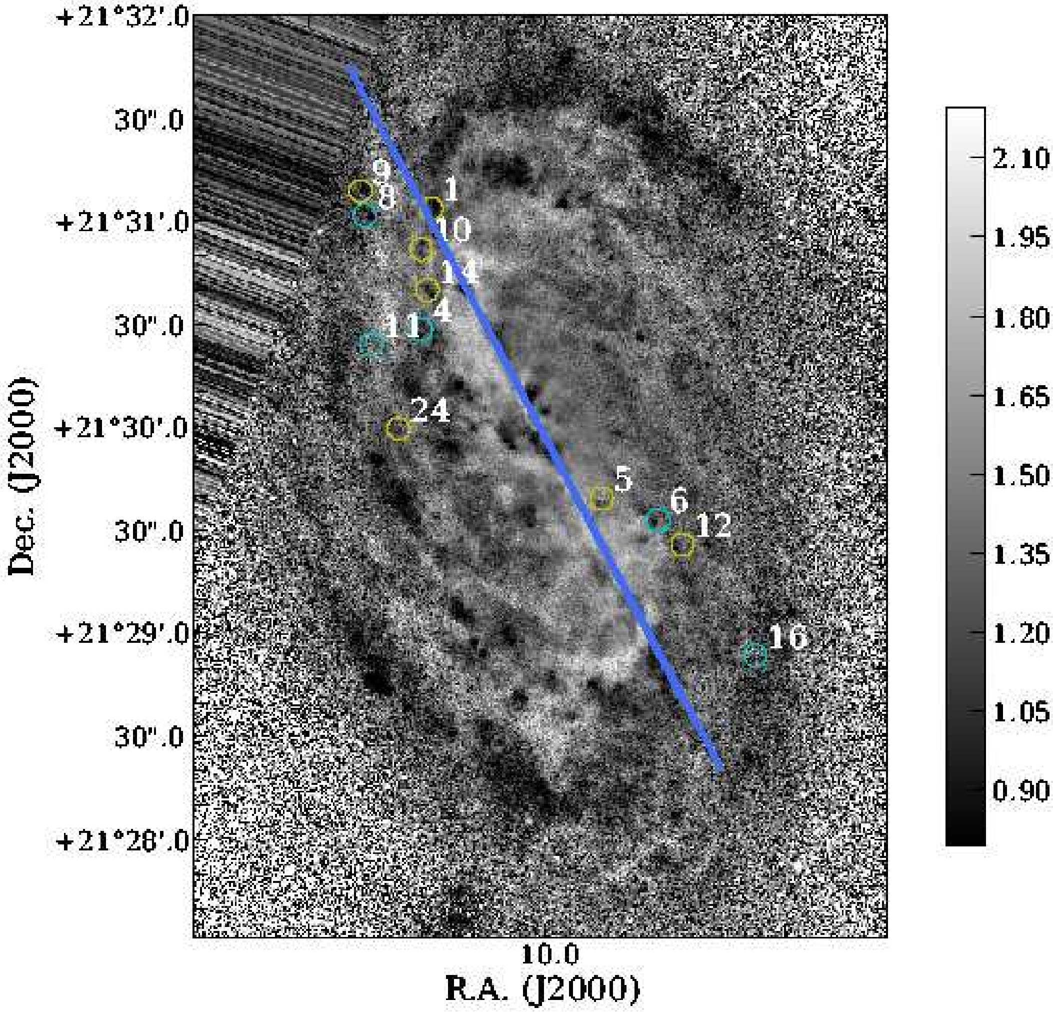

Figure 7: g'-z' colourmap of NGC 2903 in magnitudes with the Hα equivalent widths plotted on top of them. Yellow represents log EW < 2.75, cyan log EW > 2.75. The blue line represents the location of the bar.

4.1.2 EW with respect to the distance to the bar major axis and radial distance to the nucleus

As mentioned earlier, Zurita and Pérez (2008) showed for NGC 1530 that the lower EW regions sit on the leading side of the bar dust lane. We used the 3.6 microns Spitzer [5] image of NGC 2903 to determine the precise location of the bar. This observation shows a clear bar without spurs and curls as the Hα observations show (see appendix). This bar location was used to determine the distances from the HII regions to the bar major axis as projected at the sky. The obtained distances are plotted against the equivalent widths in Figure. 8.

One can clearly see two groups of EW. The first group is located within 45 arcsec from the bar major axis on the leading side (regions 5, 9, 10, 14), or close to the bar major axis at the trailing side (region 1). This group con-

[5] Spitzer Space Telescope is operated by the Jet Propulsion Laboratory, California Institute of Technology under a contract with NASA.

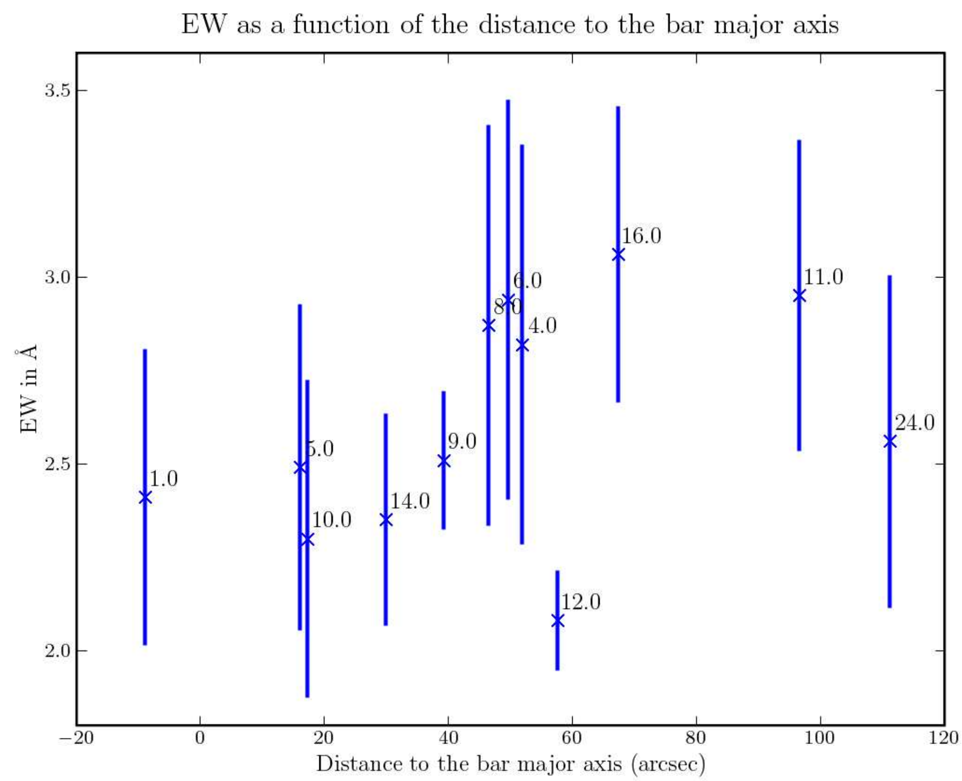

Figure 8: Hα equivalent width as function of the distance to the bar major axis as projected at the sky. One sees two groups of equivalent width distributions.

sists of HII regions with low EW. The other group consists of HII regions located further away from the bar major axis and having higher log EW values (4, 6, 8, 11, 16). This indicates the older regions to be located closer to the bar major axis.
Region 12 however, has a low EW but is located further away from the bar major axis than 45 arcsec. Region 24 as well has a low EW and is located furthest away from the bar major axis of all regions. The high EW region, however, is within the error bars of regions 24. The observed change in EW with low EW near the bar major axis is in contrary with Zurita and Pérez (2008), who found high EW regions to be located near the bar major axis.
To get a better understanding on our observed change in EW outwards from the bar major axis and to explain region 12 we will need to obtain the EW of more regions in the bar region as well as nearby in the spiral arms. HST Hα data on NGC 2903 can be used for this. Galex UV data of the bar and nearby spiral region can be used as a tracer for regions with an age up to 1 Gyr, since these regions do not emit in the Hα anymore. By use of the UV emission we can trace the movement of stellar regions through the galaxy.

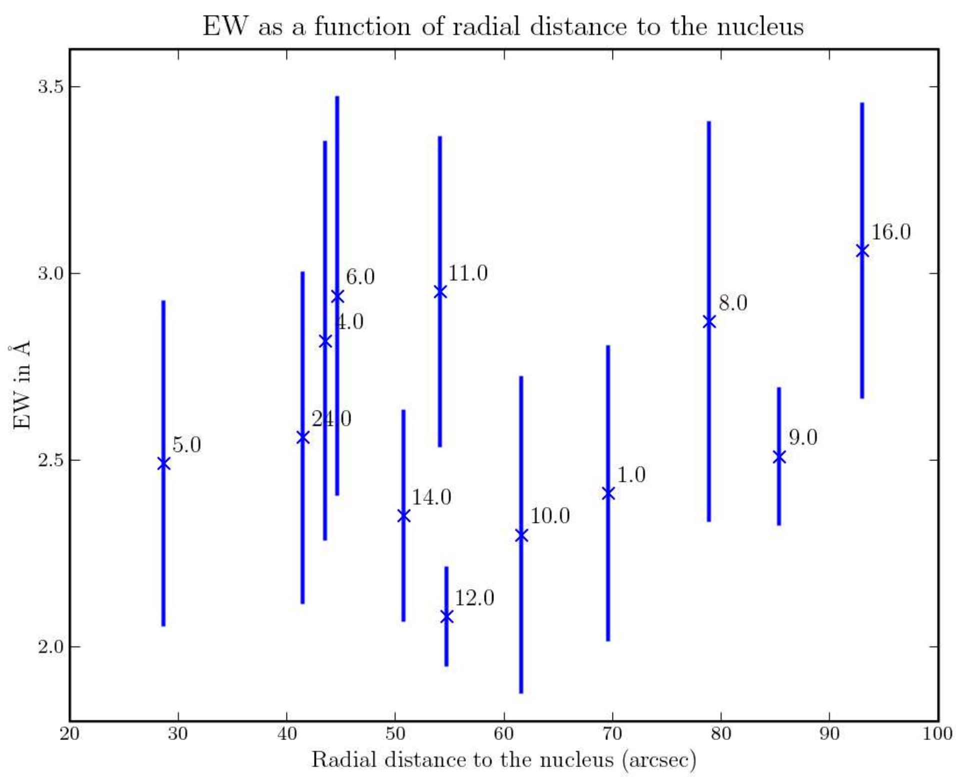

Figure 9: Hα equivalent width as a function of the radial distance to the nucleus as projected at the sky. One clearly sees a random distribution .

By use of orbital analysis and Hα velocity fields the motion of HII regions within the galaxy can be deduced and also give insight in the change in EW depending on location away from the bar major axis.
We also made a plot of the equivalent widths as a function of the radial distance to the nucleus of the galaxy as projected at the sky (Figure 9). The plot shows a random distribution of EW as a function of radial distance to the nucleus. We therefore can conclude that no correlation is present between EW and radial distance to the nucleus in the bar of NGC 2903.

5 Multiple wavelengths

Several observational programs such as SDSS, Spitzer and GALEX have released observations of NGC 2903. This gives the opportunity to do a multiple wavelength study on the star formation in the bar. Every wavelength traces different stellar and ISM properties. This can give a clearer insight in the star formation process of a galaxy.
A multiple wavelength study is especially interesting since the morphology of NGC 2903 is so complex. In the appendix images of all the observed bands can be found without countours laid on top of them. One can clearly see differences in emission location in the different bands. This might allow us to observe several regions with a different time at which a burst of star formation took place.
In this section we will discuss the Hα emission with respect to g'-z' colour map, near-UV (NUV) and far-UV (FUV) emission, near-IR (3.6 micron) and far-IR emission (24 micron) and CO emission and their consequences on star formation history.

5.1 g'-z' colourmap

Figure 10 shows the dust indicating g'-z' colour map (discussed in section 2.3) with Hα contours laid on top of it. A redder colour in the g'-z' colour map indicates more extinguished regions and therefore a dustier environment.
The bar dust lane runs from the North - West side of the nucleus to the South - East with a curl towards the end in the opposite direction as the rotational gradient of the galaxy. The bar dust lane shows a magnitude approx. 0.7 mag redder then the surrounding regions. In the southern part of the galaxy a clear dust spur can be seen approx. halfway the bar dust lane towards the trailing side reaching the bar perpendicularly. In the northern part other dusty regions can be seen towards the leading of the bar dust lane and just above the curl in the bar dust lane.
Most, and also the brightest HII regions are found on the leading side of the dust bar lane indicating star formation to take place at this side of the bar. This is in agreement with Sheth et al. (Sheth et al. 2002) and expected models (Athanassoula 1992). In the southern part of the bar bright HII regions are found between the main dust lane and the dust spur. No counterpart for this can be seen in the northern side of the bar.

5.2 Infrared

Interstellar dust absorbs a significant fraction of radiation emitted by stars. Some of this radiation is then re-emitted in the thermal IR. A part of the observed IR emission originally comes from UV representing young SF and

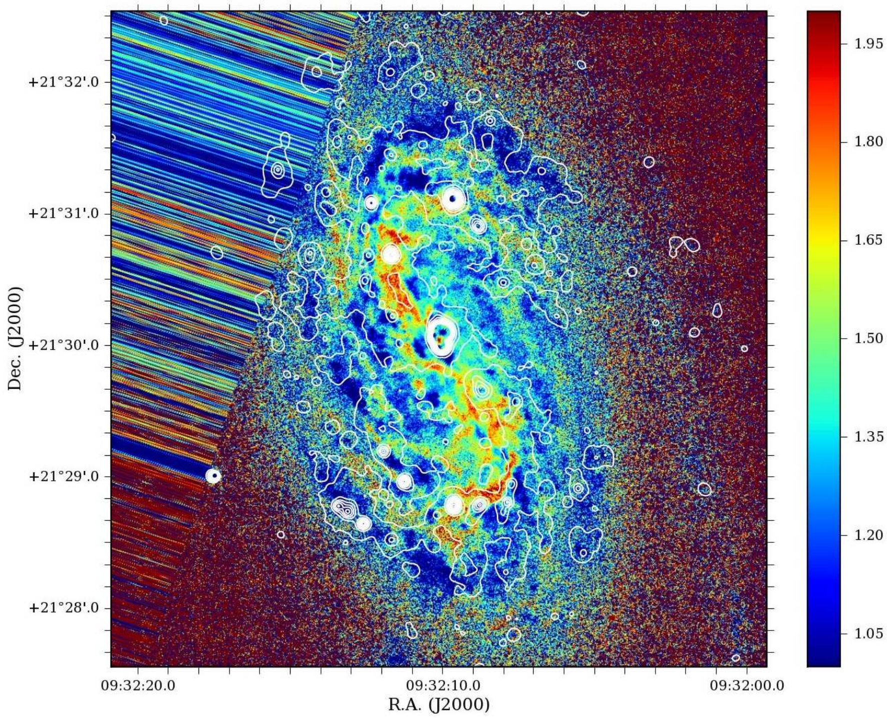

Figure 10: Hα contours plotted on top of g'-z' colour map (in magnitudes). The Hα peaks are found at the leading side of the bar dust lanes.

can therefore be used as a good SF indicator free from dust extinction.
For this project we looked at 3.6 and 24 micron observations obtained by Spitzer. Its Infrared Array Camera (IRAC) generates images in four near - IR bands with wavelengths 3.6, 4.5, 5.8 and 8 micron respectively. The Multiband Imaging Photometer for Spitzer (MIPS) generates images in three far - IR bands with wavelengths 24, 79 and 160 micron respectively. More details on Spitzer are described by Meixner et al. (Meixner et al. 2006).

5.2.1 3.6 micron

3.6 micron emission is a good tracer of stellar mass distribution free of dust obscuration effects. It therefore is a good indicator of older underlying stellar populations.
In Figure 11 the Hα contours are plotted on top of 3.6 micron observations of NGC 2903. The HII regions in the bar all show a counterpart in 3.6 micron. However, the most luminous regions in the 3.6 micron image do not show a counterpart in the Hα except for a few peaks. Especially the southern part of the bar has a luminous 3.6 micron region without a Hα counterpart. This could be because of dust absorption.

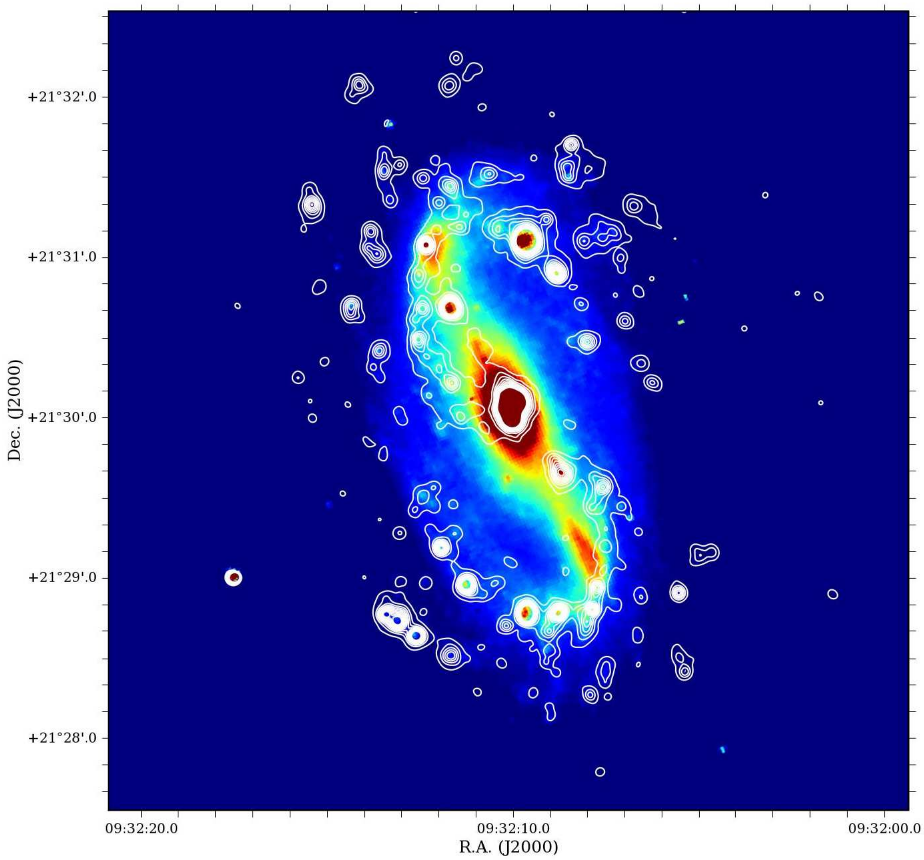

Figure 11: Hα contours plotted on top of 3.6 micron emission. Hα emission is located on the leading side of the 3.6 micron emission.

We can however conclude that HII regions in the bar of NGC 2903 tend to sit on the leading side of the bar with exception of some peaks. This indicates recent star formation in the bar of NGC 2903 to take place mostly on the leading side.

5.2.2 24 micron

Multiple studies with Spitzer data have shown 24 micron emission from pointlike sources to correspond to HII regions in optical and UV emission (Calzetti et al. 2004). Therefore the 24 micron band can be used to measure star formation activity. The 24 micron emission has the advantage not to be affected by dust attenuation. Figure 12 shows the 24 micron emission of NGC 2903 with Hα contours plotted on top of the emission. One can clearly see the HII regions fitting nicely with the 24 micron peaks, meaning that in NGC 2903 the 24 micron emission correlates with the Hα emission too.

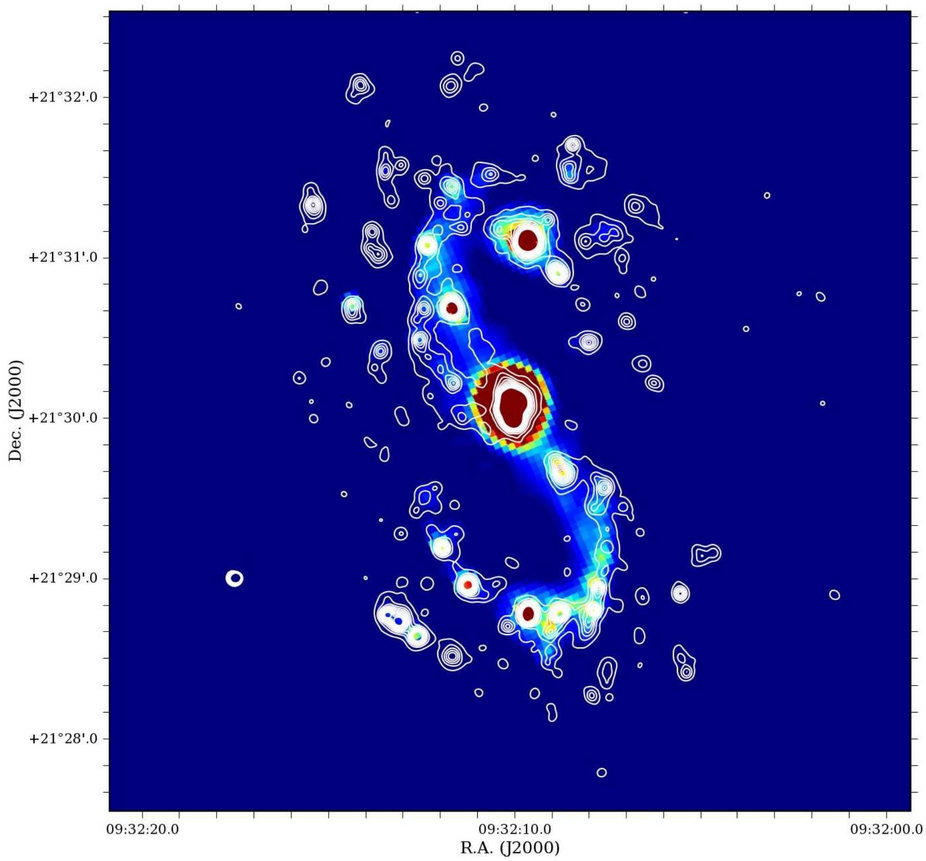

Figure 12: 24 micron contours plotted on top of Hα (in arbitrary units), they correlate nicely.

This is consistent with observations of, for example, NGC 4631 (Bendo et al. 2008) and M101 (Gordon et al. 2008).

5.3 UV data

Our UV images were obtained by GALEX[6]. GALEX surveys the sky in either imaging or spectroscopy mode. It produces a NUV and FUV image using broadband filters with effective wavelengths of 1528 and 2271 Å respectively. First we will discuss the NUV observations of NGC 2903, then the FUV observations.

[6]GALEX is a NASA mission managed by the Jet Propulsion Laboratory

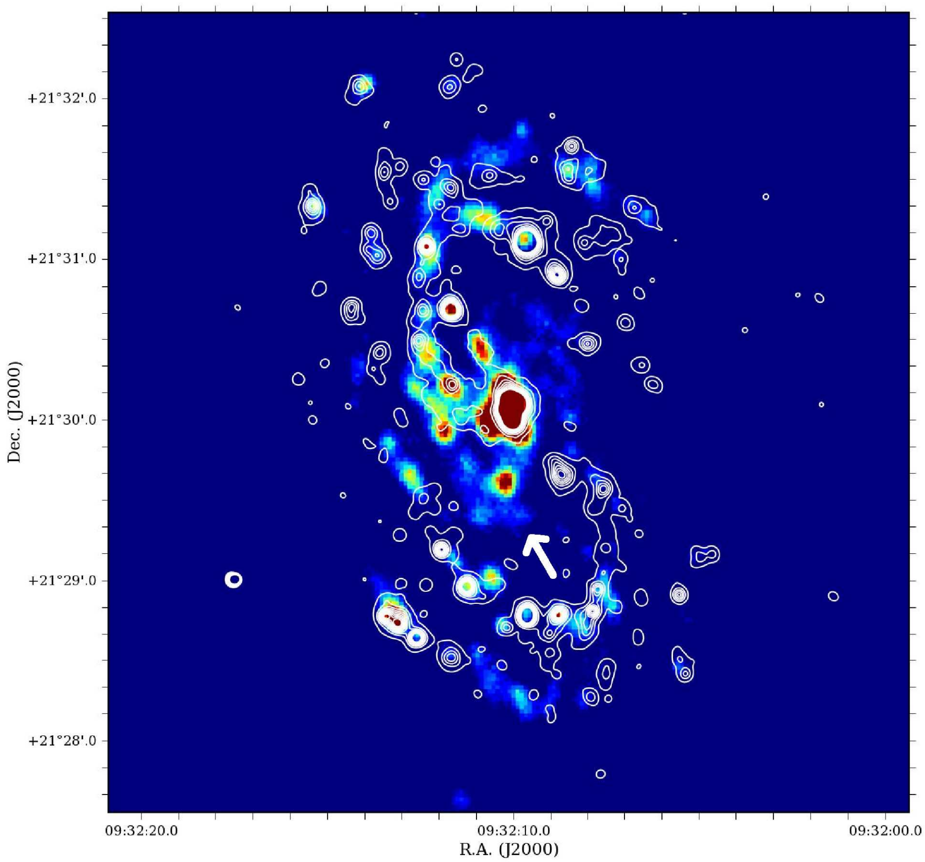

Figure 13: NUV contours plotted on top of Hα (in arbitrary units). A clear NUV region with no Hα counterpart is located to the South of the nucleus, this region is indicated with the arrow.

5.3.1 NUV

The NUV is a tracer of recent SF. Figure 13 shows Hα contours on top of NUV emission.

In the northern part of the galaxy the Hα peaks follow the NUV rather nicely. At the southern part the NUV regions seem to be located a bit to the leading side of the Hα. This could be an indication of migrating earlier formed stars towards the leading side. Stars travel away from the SF sites, since they have their own orbiting motion in the bar. As older stars have had more time to migrate within the bar, it is expected to see a migration from the earlier formed stars away from recent star forming regions.

Just to the South of the nucleus a clear NUV region is located without a counterpart in the Hα, this region is indicated with the white arrow. Extinction has a larger effect on NUV than on Hα, NUV and Hα having an optical depth of 4 and 2.4 respectively (Calzetti et al. 1994). This implies that Hα, if present, cannot be obscured by dust when NUV emission is observed, as NUV would be obscured earlier. For M81 it is shown that age difference is sufficient to explain star-forming regions both detected in Hα and UV and those detected only in UV (Gogarten et al. 2008). This indicates that our region with no Hα counterpart is an earlier burst of SF without current ionized gas emission counterpart.

We do not see this NUV region correlating with the bar morphology. As Hα traces places where bar dynamics favour SF (ie. the bar dominates the dynamics in the inner disk) and the NUV does not correlate with the Hα, we can conclude that the UV does not seem to be associated to the dynamical features of the bar. As stars orbit within the bar, we would expect older population stars to be located in this UV region too. This would imply the stars traced by the UV and older population stars to have been formed at

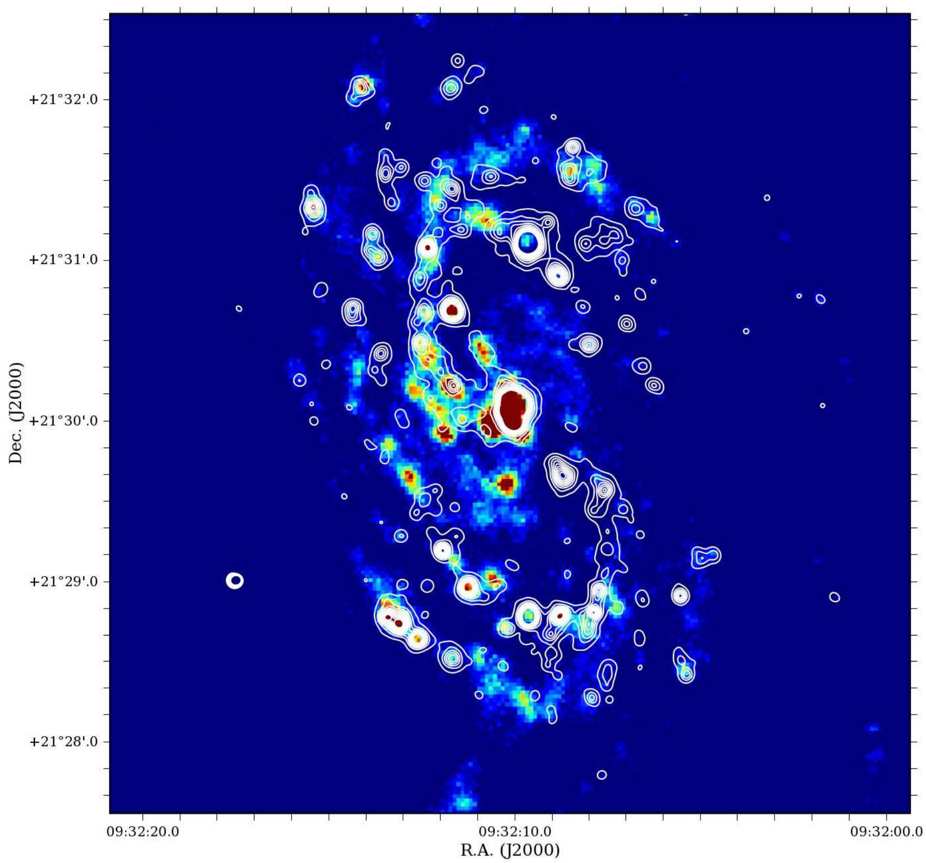

Figure 14: FUV contours plotted on top of Hα (in arbitrary units). A clear FUV peak with no Hα counterpart is located to the South of the nucleus.

the same location in the bar. Since we do not see these older population stars in this UV region, we can conclude that the stars traced by the UV formed at different locations. This SF of the stars traced by the UV could be triggered by the formation of the bar, since we expect a global SF burst in the inner disk at the epoch of bar formation. This would imply that the bar of NGC 2903 has been formed less than 1 Gyr ago. This SF burst cannot be triggered by merging with a smaller object, since HI emission shows regular velocity fields (Irwin et al. 2008). Further investigations will be necessary to get a better understanding on the formation of the bar of NGC 2903.

5.3.2 FUV

FUV is a good tracer of evolved hot stars (up to ~ 1 Gyr). Figure 14 shows Hα contours on top of FUV observations. Clear peaks in the UV can be seen at the North - East part of the nucleus. These peaks correlate nicely

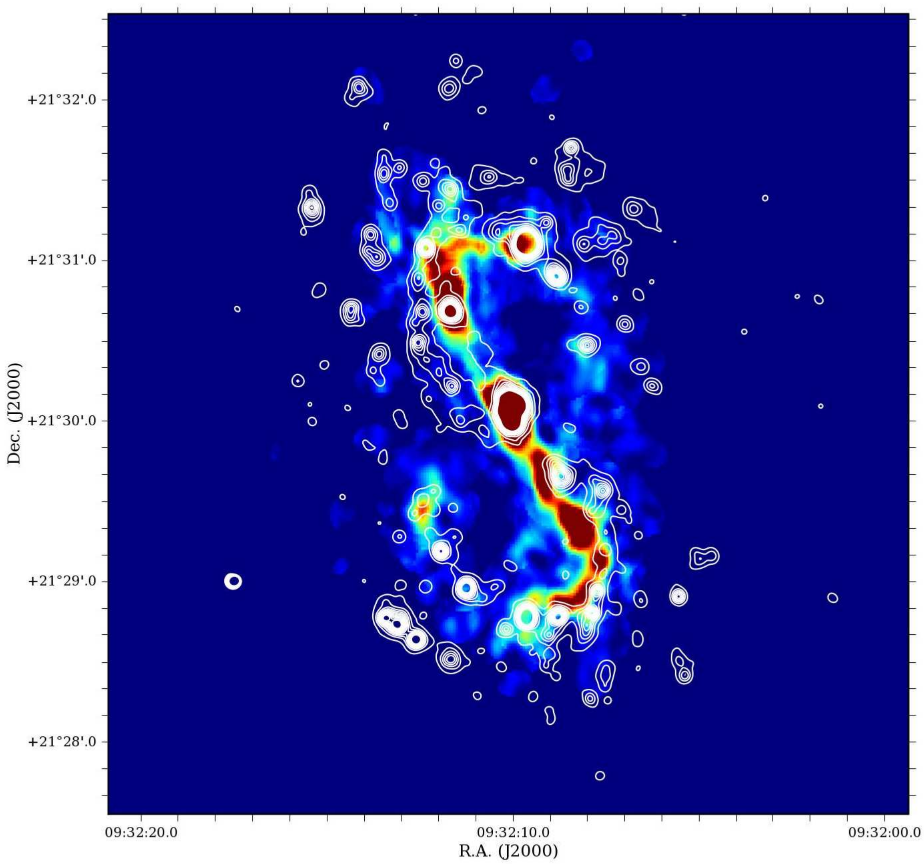

Figure 15: CO(1-0) contours plotted on top of Hα (in arbitrary units). The Hα emission is nicely located at the trailing side of the CO emission.

with the 24 micron FIR observations, which should be the case since the IR shows re-emitted UV emission. The FUV also shows clear peaks in the North - East part at the same places as the Hα peeks. Not all FUV peaks have a Hα region around them.
In the region to the South of the nucleus no correlation can be seen between the FUV and 24 micron IR and the FUV and Hα emission. One clear peak just to the South of the nucleus is present with no counterpart in the Hα, again indicating earlier SF with no recent or current counterpart. For FUV also the exctinction rate is higher than for Hα, therefore the Hα cannot be obscured by dust since we see FUV emission.

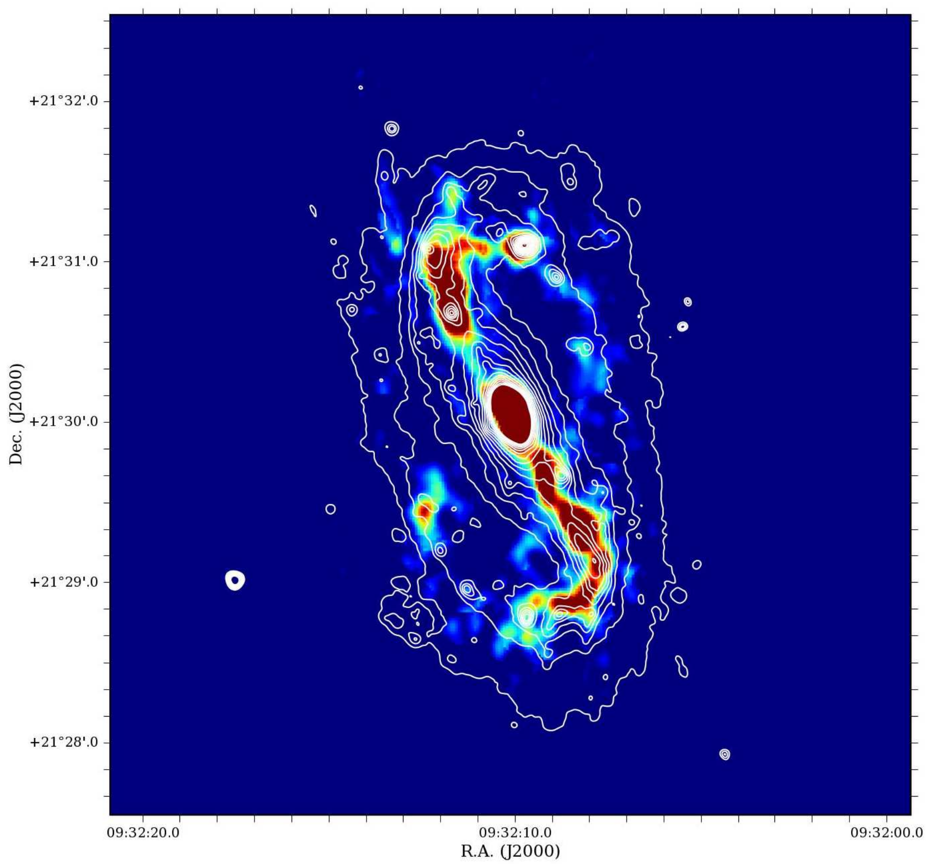

Figure 16: 3.6 micron emission contours plotted on top of CO(1-0). The 3.6 micron emission correlates nicely with the CO in the bar region. This might indicates SF taking place on top of older stellar populations, suggesting multiple populations.

5.4 CO

Massive clouds containing much of a galaxy's interstellar medium are the precursors of star formation. CO emission represents these moderate dense clouds and therefore is a good indicator on the location where SF could be happening.
For comparing our Hα observation with CO data we used data kindly provided to us by Ute Lisenfeld as mentioned earlier. The observation was done as a part of the BIMA-Song survey (Helfer et al. 2003) and maps the CO(1-0) emission in NGC 2903 at a resolution of 6". The Hα contours are plotted on top of the CO data in Figure 15.
As well as for the 3.6 micron case, most HII regions sit on the edge of the CO peaks. This is in agreement with "the blister model" (Israel 1978), which states HII regions to form at the edges of CO clouds and the CO to follow the bar.
Figure 16 shows 3.6 micron emission plotted on top of CO emission. We clearly see that the 3.6 micron emission correlates nicely with the CO emission in the bar region.

6 Conclusions

We did a careful analysis of the properties of the HII regions in the bar of NGC 2903. We examined the EW of the HII regions as a function of the location with respect to the bar dust lane, distance to the bar major axis and the radial distance to the nucleus. We compared these results to NGC 1530, where clear differences were found in the EW of HII regions dependant on their position with respect to the bar dust lane. We also discussed the properties of the bar in different bands (g'-z' colourmap, NUV, FUV, NIR, FIR and CO) and compared them to each other, to get a further insight into its star forming history. Our main conclusions are:

- NGC 2903 has a bar with a complex morphology in different bands. The g'-z' colourmap indicates that the dust is distributed not only along the bar, but also in spurs and isolated regions. The UV, IR, CO and Hα all show emission at different places, not always correlating with each other.

- The HII regions all tend to sit at the leading side of the bar dust lane, or close to the bar major axis at the trailing side, as predicted by earlier models and observations.

- We found no correlation between the $EW_{H\alpha}$ of HII regions and their location on the leading or trailing side with respect to the bar dust lane.

- We found no correlation between the $EW_{H\alpha}$ of the HII regions and their radial distance to the nucleus. Looking at their perpendicular distances to the bar major axis we found a change in EW around a distance 45 arcsec away from the bar major axis at the leading side. Regions close to the bar major axis have a low EW, whereas further away from the bar major axis they have a high EW.

- Zurita and Pérez (2008) found for NGC 1530 HII regions to be present both at the leading and trailing side with respect to the bar dust lane. They were the first to do a study on the relation between $EW_{H\alpha}$ and the distance to the bar major axis and found clear differences in EW of HII regions depending on location, with HII regions at the far leading side of the bar having a low EW. We found the opposite, indicating that the bars might have a difference SF history.

- In the UV we see a clear region without a counterpart in the Hα and not correlating with the bar region. As Hα traces places where bar dynamics favour SF (ie. the bar dominates the dynamics in the inner disk) and the NUV does not correlate with the Hα, we can conclude that the UV does not seem to be associated to the bar dynamical features. As stars orbit within the bar, we would expect older population stars to be located in this UV region too. This would imply the stars traced by the UV and older population stars to have been formed at the same location in the bar. Since we do not see these older population stars in this UV region, we can conclude that the stars traced by the UV formed at different locations. The SF of the stars traced by the UV could be triggered by the formation of the bar, since we expect a global SF burst in the inner disk at the epoch of bar formation. This would imply that the bar of NGC 2903 has been formed less than 1 Gyr ago. This SF burst cannot be triggered by merging with a smaller object, since HI emission shows regular velocity fields (Irwin et al. 2008). Further investigations will be necessary to get a better understanding on the formation of the bar of NGC 2903.

- We found some UV emission to be placed just to the leading side of some HII regions. This could indicate migrating earlier formed stars away from the HII regions. This is expected as stars travel through the bar because of the orbital motion in the bar.

We believe the UV region without a counterpart in the Hα and not correlating with the bar morphology in other bands, might indicate a recently formed bar. This can give great new insight into the formation of barred spirals. A more detailed research on this region taking into account the stellar populations, dust distribution and dynamics will be necessary for better understanding bar formation.
Calculating the EW of a larger amount of HII regions in the bar of NGC 2903 as well as nearby in the spiral arms, combined with UV data tracing star forming regions up to 1 Gyr, velocity fields and orbital analysis could give a better insight in the observed change in EW.

7 Acknowledgements

I would like to thank my supervisors Isabel Pérez-Martin and Almudena Zurita for all the help during this project, for the nice discussions, introducing me into the world of barred spirals and into doing research. I'm also very grateful for them inviting me to Granada, taking me snorkeling and helping me out with the Alhambra tickets.
I would also like to thank Reynier Peletier for his useful comments on the report, it certainly helped improving the final work.

References

E. Athanassoula. The existence and shapes of dust lanes in galactic bars. *MNRAS*, 259:345–364, November 1992.

R. Beck. *in Disks of Galaxies: Kinematics, Dynamics and Perturbations, Athanassoula, L., Bosma, A., Mujica, R. (eds).* ASP Vonf. ser. 275, San Francisco, p. 331, 2002.

G. J. Bendo, B. T. Draine, C. W. Engelbracht, G. Helou, M. D. Thornley, C. Bot, B. A. Buckalew, D. Calzetti, D. A. Dale, D. J. Hollenbach, A. Li, and J. Moustakas. The relations among 8, 24 and 160 μm dust emission within nearby spiral galaxies. *MNRAS*, 389:629–650, September 2008.

D. Calzetti, R. C. Kennicutt, M. Meyer, M. L. Sosey, M. Mutchler, M. Regan, L. Bianchi, D. Thilker, C. Hoopes, C. W. Engelbracht, G. Bendo, K. D. Gordon, G. H. Rieke, M. J. Rieke, M. Thornley, G. Helou, P. G. Friedman, M. Polletta, N. Z. Scoville, S. Boissier, A. Boselli, L. Kewley, F. Walter, and S. K. Yi. Star Formation in NGC5194 (M51): A Panchromatic Investigation from Spitzer to GALEX. In *Bulletin of the American Astronomical Society*, volume 36 of *Bulletin of the American Astronomical Society*, pages 1442–+, December 2004.

D. Calzetti, A. L. Kinney, and T. Storchi-Bergmann. Dust extinction of the stellar continua in starburst galaxies: The ultraviolet and optical extinction law. *ApJ*, 429:582–601, July 1994.

C. Giammanco, J. E. Beckman, A. Zurita, and M. Relaño. Propagation of ionizing radiation in H II regions: The effects of optically thick density fluctuations. *A&A*, 424:877–885, September 2004.

S. M. Gogarten, J. J. Dalcanton, B. F. Williams, A. C. Seth, A. Dolphin, D. Weisz, E. Skillman, J. Holtzman, A. Cole, L. Girardi, R. S. de Jong, I. D. Karachentsev, K. Olsen, and K. Rosema. The ACS Nearby Galaxy Survey Treasury II. Young Stars and their Relation to Halpha and UV Emission Timescales in the M81 Outer Disk. *ArXiv e-prints*, October 2008.

K. D. Gordon, C. Engelbracht, J. D. T. Smith, G. Rieke, and K. Misselt. *Arxiv e-prints*, 2008.

T. T. Helfer, M. D. Thornley, M. W. Regan, T. Wong, K. Sheth, S. N. Vogel, L. Blitz, and D. C.-J. Bock. The BIMA Survey of Nearby Galaxies (BIMA SONG). II. The CO Data. *ApJS*, 145:259–327, April 2003.

J. A. Irwin, G. L. Hoffman, K. Spekkens, M. P. Haynes, R. Giovanelli, S. M. Linder, B. Catinella, E. Momjian, B. S. Koribalski, J. Davies, E. Brinks,

W. J. G. de Blok, M. E. Putman, and W. van Driel. LCDM Satellites and HI Companions - The Arecibo ALFA Survey of NGC 2903. *ArXiv e-prints*, October 2008.

F. P. Israel. H II regions and CO clouds - The blister model. *A&A*, 70: 769–775, December 1978.

C. Leitherer, D. Schaerer, J. D. Goldader, R. M. G. Delgado, C. Robert, D. F. Kune, D. F. de Mello, D. Devost, and T. M. Heckman. Starburst99: Synthesis Models for Galaxies with Active Star Formation. *ApJS*, 123: 3–40, July 1999.

P. Martin and D. Friedli. Star formation in bar environments regions. II. Physical properties, age and abundances of H II. *A&A*, 346:769–777, June 1999.

Y. D. Mayya. Embedded clusters in giant extragalactic H II regions, 1: BVRH-alpha photometry. *ApJ*, 108:1276–1291, October 1994.

M. Meixner, K. D. Gordon, R. Indebetouw, J. L. Hora, B. Whitney, R. Blum, W. Reach, J.-P. Bernard, M. Meade, B. Babler, C. W. Engelbracht, B.-Q. For, K. Misselt, U. Vijh, C. Leitherer, M. Cohen, E. B. Churchwell, F. Boulanger, J. A. Frogel, Y. Fukui, J. Gallagher, V. Gorjian, J. Harris, D. Kelly, A. Kawamura, S. Kim, W. B. Latter, S. Madden, C. Markwick-Kemper, A. Mizuno, N. Mizuno, J. Mould, A. Nota, M. S. Oey, K. Olsen, T. Onishi, R. Paladini, N. Panagia, P. Perez-Gonzalez, H. Shibai, S. Sato, L. Smith, L. Staveley-Smith, A. G. G. M. Tielens, T. Ueta, S. V. Dyk, K. Volk, M. Werner, and D. Zaritsky. Spitzer Survey of the Large Magellanic Cloud: Surveying the Agents of a Galaxy's Evolution (SAGE). I. Overview and Initial Results. *ApJ*, 132:2268–2288, December 2006.

W. D. Pence and C. P. Blackman. Dynamics of gas in barred spiral galaxies. I - NGC 6221. *MNRAS*, 207:9–23, March 1984.

M. Relaño, J. E. Beckman, A. Zurita, M. Rozas, and C. Giammanco. The internal dynamical equilibrium of H II regions: A statistical study. *A&A*, 431:235–251, February 2005.

D. Reynaud and D. Downes. Kinematics of the gas in a barred galaxy: do strong shocks inhibit star formation? *A&A*, 337:671–680, September 1998.

M. Rozas, A. Zurita, and J. E. Beckman. The ionized gas in the spiral galaxy NGC 3359. I. Photometry. *A&A*, 354:823–835, February 2000.

K. Sheth, S. N. Vogel, M. W. Regan, P. J. Teuben, A. I. Harris, and M. D. Thornley. Molecular Gas and Star Formation in Bars of Nearby Spiral Galaxies. *ApJ*, 124:2581–2599, November 2002.

S. Verley, F. Combes, L. Verdes-Montenegro, G. Bergond, and S. Leon. Star formation in isolated AMIGA galaxies: dynamical influence of bars. *A&A*, 474:43–53, October 2007.

A. Zurita and I. Pérez. Where are the stars of the bar of NGC 1530 forming? *A&A*, 485:5–20, July 2008.

A Appendix

Images of NGC 2903 in different bands:

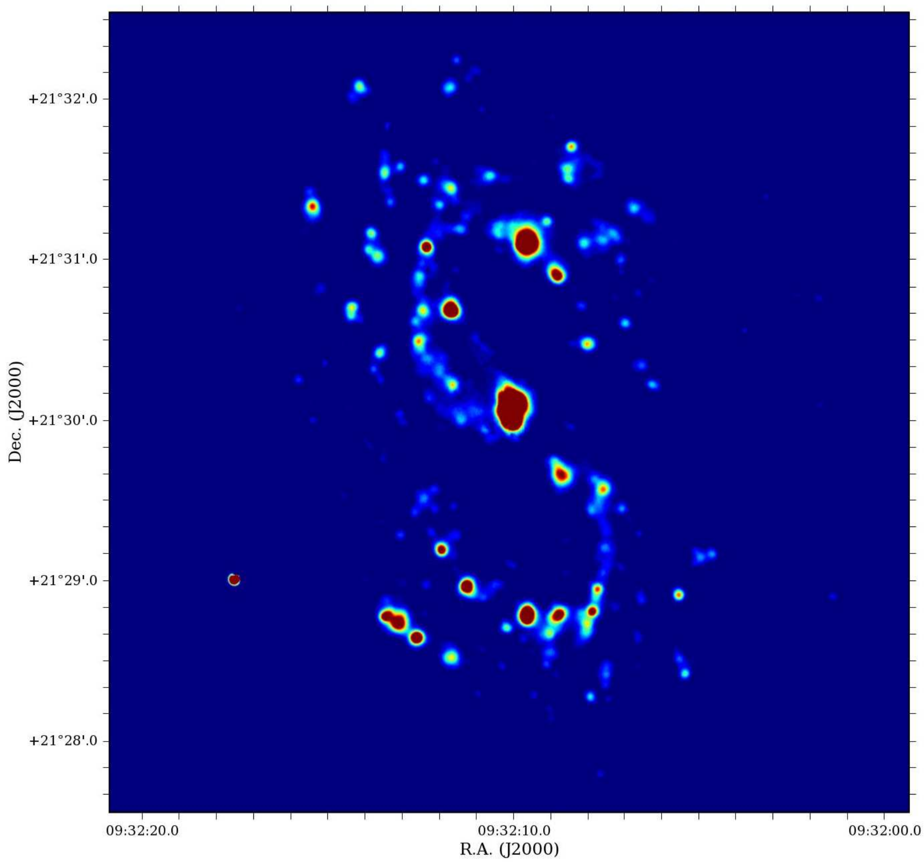

Figure 17: Hα image of NGC 2903

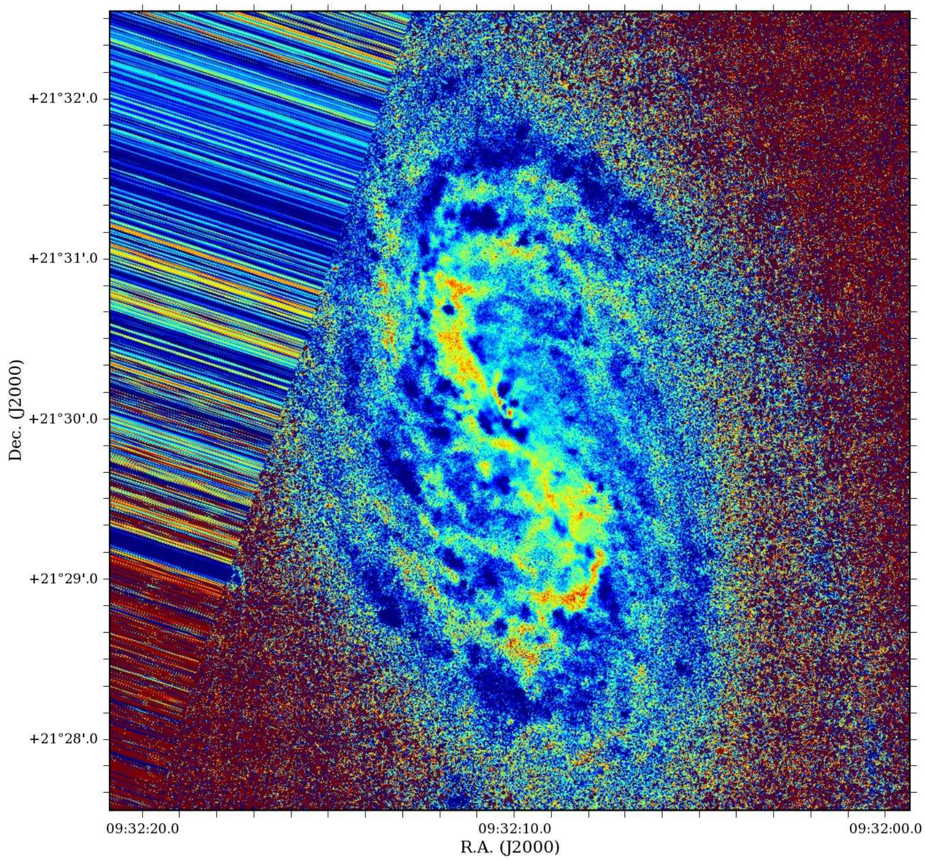

Figure 18: g'-z' colour map of NGC 2903

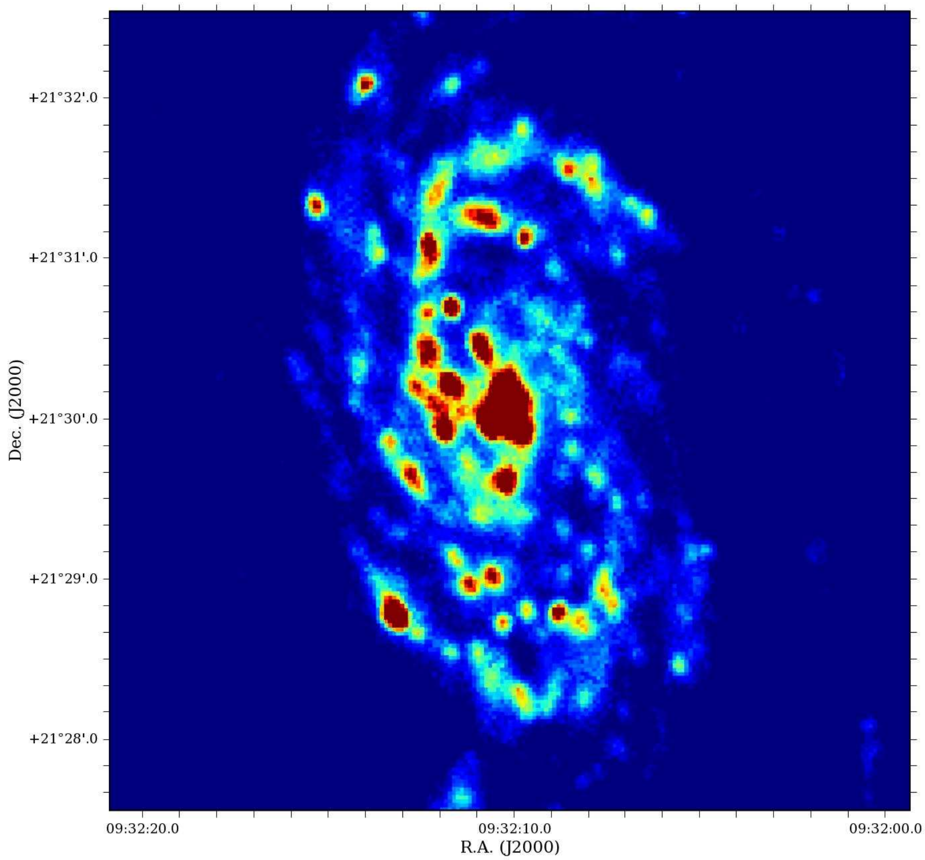

Figure 19: NUV observation of NGC 2903

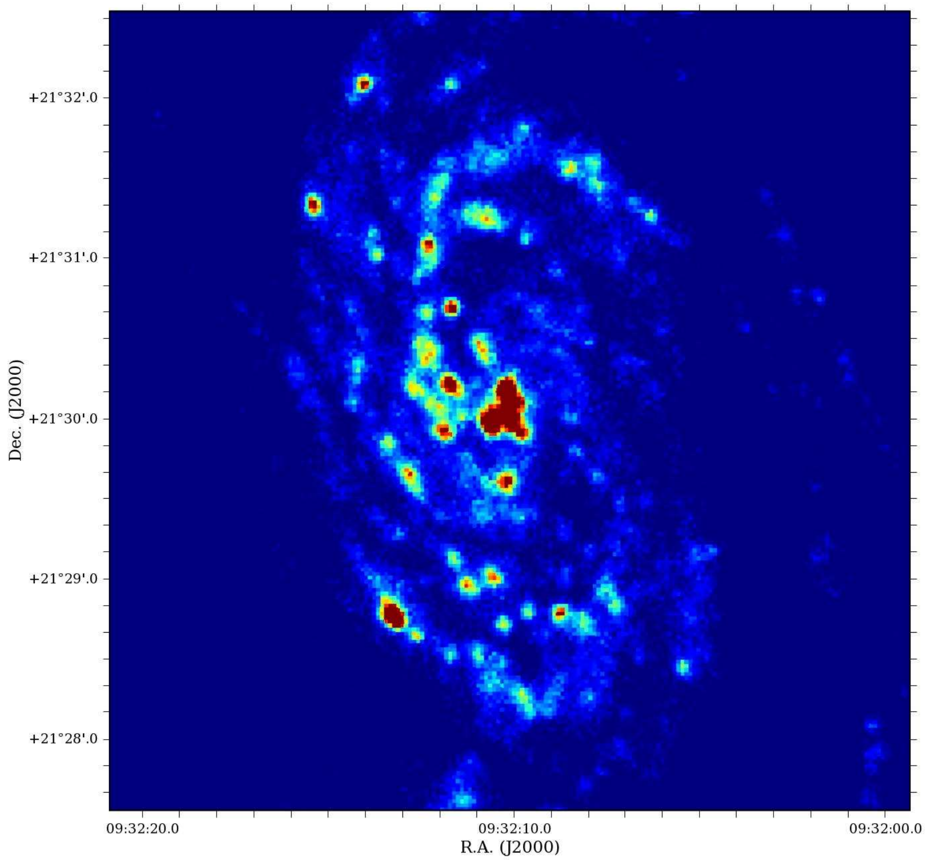

Figure 20: FUV observation of NGC 2903

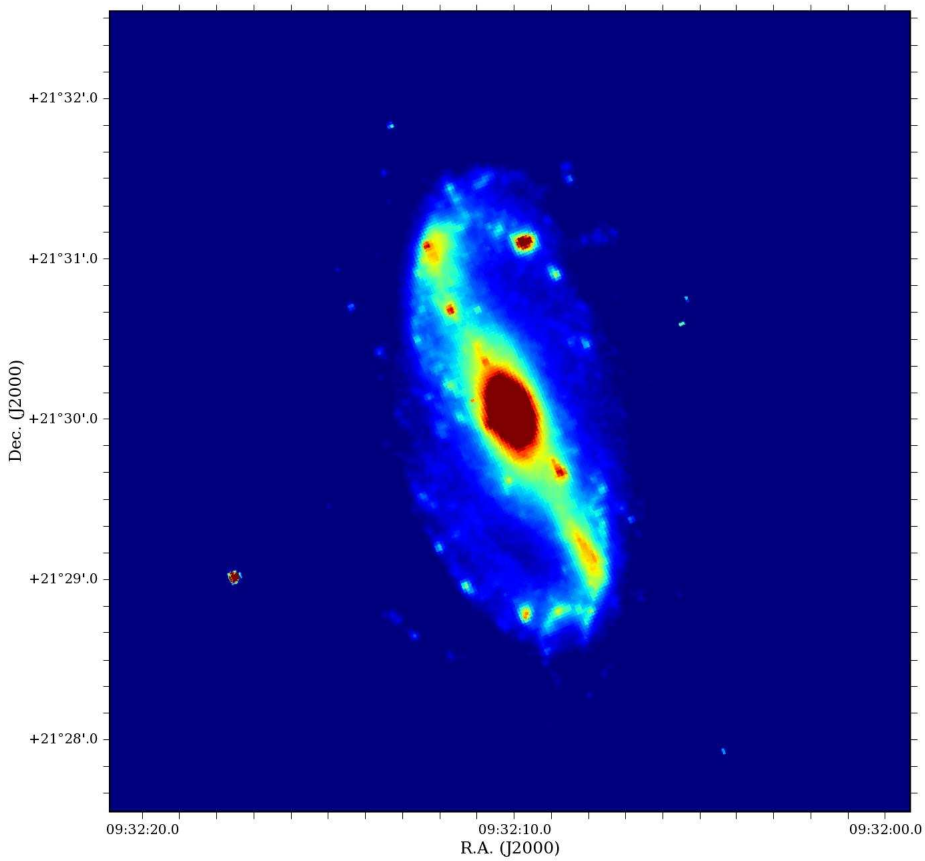

Figure 21: 3.6 micron emission observation of NGC 2903

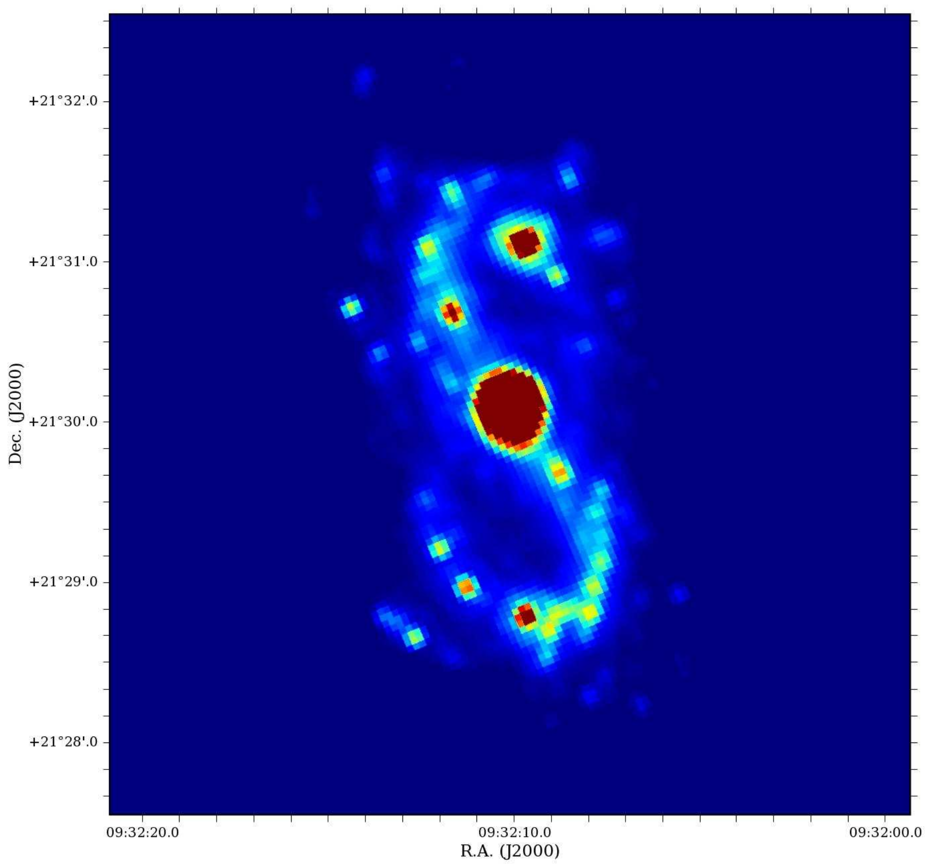

Figure 22: 24 micron emission observation of NGC 2903

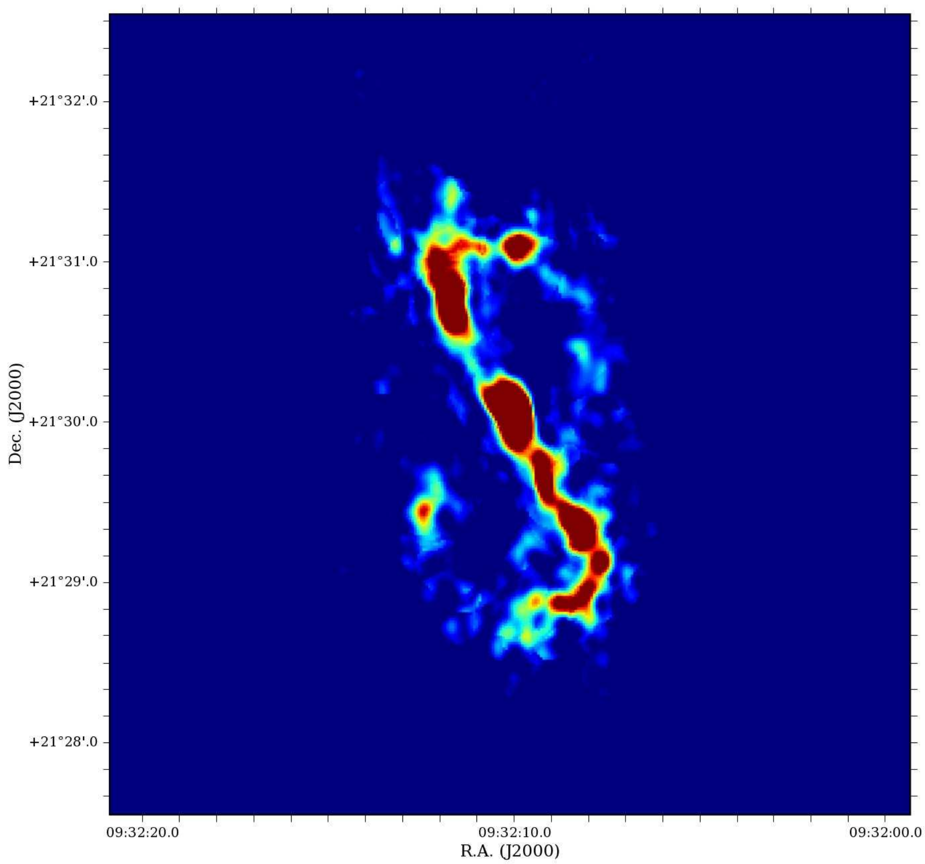

Figure 23: CO emission observation of NGC 2903